PHOTONICS Research

Experimental demonstration of coherent photonic neural computing based on a Fabry–Perot laser with a saturable absorber

Dianzhuang Zheng,[1] Shuiying Xiang,[1,2,6] Xingxing Guo,[1] Yahui Zhang,[1] Biling Gu,[1] Hongji Wang,[3] Zhenzhen Xu,[3] Xiaojun Zhu,[4] Yuechun Shi,[3,5,7] and Yue Hao[2]

[1]State Key Laboratory of Integrated Service Networks, Xidian University, Xi'an 710071, China
[2]State Key Discipline Laboratory of Wide Band Gap Semiconductor Technology, School of Microelectronics, Xidian University, Xi'an 710071, China
[3]Key Laboratory of Intelligent Optical Sensing and Manipulation, Ministry of Education, National Laboratory of Solid State Microstructures, College of Engineering and Applied Sciences, Institute of Optical Communication Engineering, Nanjing University, Nanjing 210023, China
[4]School of Information Science and Technology, Nantong University, Nantong 226019, China
[5]Yongjiang Laboratory, Ningbo 315202, China
[6]e-mail: syxiang@xidian.edu.cn
[7]e-mail: yuechun-shi@ylab.ac.cn

Received 1 August 2022; revised 5 November 2022; accepted 8 November 2022; posted 8 November 2022 (Doc. ID 471950); published 23 December 2022

As Moore's law has reached its limits, it is becoming increasingly difficult for traditional computing architectures to meet the demands of continued growth in computing power. Photonic neural computing has become a promising approach to overcome the von Neuman bottleneck. However, while photonic neural networks are good at linear computing, it is difficult to achieve nonlinear computing. Here, we propose and experimentally demonstrate a coherent photonic spiking neural network consisting of Mach–Zehnder modulators (MZMs) as the synapse and an integrated quantum-well Fabry–Perot laser with a saturable absorber (FP-SA) as the photonic spiking neuron. Both linear computation and nonlinear computation are realized in the experiment. In such a coherent architecture, two presynaptic signals are modulated and weighted with two intensity modulation MZMs through the same optical carrier. The nonlinear neuron-like dynamics including temporal integration, threshold, and refractory period are successfully demonstrated. Besides, the effects of frequency detuning on the nonlinear neuron-like dynamics are also explored, and the frequency detuning condition is revealed. The proposed hardware architecture plays a foundational role in constructing a large-scale coherent photonic spiking neural network.

https://doi.org/10.1364/PRJ.471950

1. INTRODUCTION

With the rapid development of artificial intelligence (AI) technology, it is increasingly difficult to meet the computational power required to train AI models with conventional electronic processors based on von Neumann's architecture [1]. The well-known Moore's law seems to be slowing down [2]. The computation power of integrated electronic circuits is also hardly sufficient to cope with the rapidly increasing volume of data. Neuromorphic computing holds the promise of breaking through traditional computing to achieve increased computing power and reduced power consumption. Some electronic neuromorphic processors such as the TrueNorth [3], SpiNNaker [4], and Loihi [5] have been developed to show superb computing power. Due to the inherent advantages of light in terms of high speed, wide bandwidth, and low electromagnetic interference, neuromorphic computing has been developed rapidly and efficiently in the field of optics [6–10]. Neuromorphic photonics will have a huge and far-reaching impact in the field of AI [9–11]. Compared with classical computing, photonics neuromorphic computing [7–12] offers the advantages of high bandwidth, massive parallel computing, and ultra-low energy consumption, making it suitable for deep-learning-type tasks such as speech recognition, target detection [13–17], and edge-computing applications [18].

The photonic circuits that enable neuromorphic computing are composed of a large number of photonic devices, which need to be matched to existing established neural network frameworks. With the development of photonic integration technology, significant progress has been made in the hardware implementation of photonic neural networks. Inspired by the biological brain, the neuromorphic photonic structure consists of photonic neurons and synapses. Since semiconductor lasers

can generate complex neuron-like dynamics, a large number of semiconductor laser-based approaches have been proposed to simulate spiking laser neurons experimentally and numerically [19–24]. Spiking laser neurons consist of two main types: optical/electrical/optical (O/E/O) neurons [25] and all-optical neurons [19,20,23,24]. Two-section excitable lasers [19–21, 24–27], vertical cavity surface-emitting lasers (VCSELs) [23,28–30], resonant tunneling diodes [19,22,31,32], micropillar lasers [19,33,34], and modulator-based neurons [35,36] have all been used to emulate the photonic neurons.

To date, optical neural network architectures for linear operation fall into two main categories: wavelength-division-multiplexed (WDM) layout [9,37–39] and coherent interference schemes [7,40–42]. A photonic neural network based on the WDM scheme uses different wavelengths to encode the input signals. That is to say, each photonic synapse is implemented using a different wavelength. However, achieving precise resonant control [39] can be difficult. One approach is to use a single light source that can produce multiple wavelengths, which requires a complex process and a high cost [43].

Coherent neural networks hold the promise of leveraging existing integrated interferometric platforms to enable large-scale integrated photonic chips. Currently, coherent photonic neural networks with multiple cascaded Mach–Zehnder interferometers (MZIs) have been successfully implemented theoretically and experimentally [7,44,45]. Shen *et al.* used cascaded MZIs to simulate artificial neural networks to implement deep learning tasks [7]. Zhou *et al.* have designed reconfigurable photonic signal processors using MZI lattices, which can implement a variety of complex optical functions [45]. The delay and weighting of signals by synapses are a learning mechanism in the biological brain, and there are few hardware architectures available to simulate its implementation [46]. However, while photonic neural networks are good at linear computing, it is difficult to achieve nonlinear computing. Specifically, a prototypical photonic spiking neural network that includes both the photonic synapses and photonic neurons for neural computation remains unexplored.

In this work, we propose and experimentally demonstrate a prototypical photonic coherent spiking neural network consisting of Mach–Zehnder modulators (MZMs) as the photonic synapse and the integrated quantum-well Fabry–Perot laser with a saturable absorber (FP-SA) as the photonic spiking neuron. The main advantages of using FP-SA are as follows. Compared to the VCSEL-SA and optically injected VCSEL without SA [23,27–29], the FP-SA is easy to fabricate with a simple commercial process. Besides, the output power is much larger than that of the VCSEL-SA and VCSEL; thus, it is highly desirable for future integration with the synapse. Compared to the silicon ring-based spiking neuron [47], the response speed of the FP-SA is faster due to the fast carrier dynamics inside the laser cavity. In addition, the FP-SA is a multi-longitudinal mode laser, which will enable wavelength-multiplexing computing and, thus, increase the computing speed. Furthermore, the FP-SA can be easily controlled with gain current and reverse voltage, which makes the FP-SA a reconfigurable spiking neuron. In the proposed coherent photonic spiking neural network architecture, two presynaptic signals are weighted with two electro-optical intensity modulators through the same optical carrier. We have obtained different weighted summation signals by adjusting the electrical delay of the input signals and voltages of the MZMs and phase shifter. The weighted sum is then injected into the FP-SA that serves as the photonic spiking neuron. The experimental results show that the hardware architecture can realize the nonlinear neuron-like dynamics including temporal integration, threshold, and refractory period to accomplish nonlinear computations. Besides, the effects of frequency detuning between the injected light and the FP-SA on the nonlinear neuron-like dynamics are also explored.

2. EXPERIMENT SETUP AND METHOD

Coherent photonic neural networks use interference between coherent optical fields for weighted summation operations. The schematic diagram of the proposed hardware architecture is shown in Fig. 1. It is composed of three neurons, i.e., two presynaptic neurons (PRE) and one postsynaptic neuron (POST), and two synapses (W_1 and W_2) connecting the neurons. The electronic signal from one of the PRE outputs is delayed. The electronic signals from the two PRE outputs are electro-optically converted and weighted by two MZMs. The experimental setup for the schematic diagram of the photonic coherent spiking neural network is shown in Fig. 2(a). Here, the photonic synapses that perform linear computation are marked with the green block, and the photonic spiking neurons that perform nonlinear computation are marked with the red block. More specifically, two channel signals generated by the arbitrary waveform generator (AWG) are adopted to mimic two PRE outputs, respectively, and the FP-SA is employed to emulate the POST. The differential quadrature reference phase shift keying (DQPSK) MZM is used to mimic the optical synapse. Here, the quantum-well FP-SA was designed and fabricated, as shown in Fig. 2(b). The epitaxy structure of the wafer is similar to that in Ref. [48].

In the experiments, a tunable laser (TL, AQ2200-136 TLS module) operated in the continuous-wave (CW) state. The polarization state of the light could be adjusted by the polarization controller (PC). Two output signals, Vin1 and Vin2, shown in Fig. 2(c), originating from the AWG (Tektronix AWG70001A), were forwarded to two electronic amplifiers to drive two MZMs. One of the input signals has been delayed. The output of the TL was divided into two identical copies and recombined again after modulation to form the weighted summation. The two presynaptic signals were modulated and

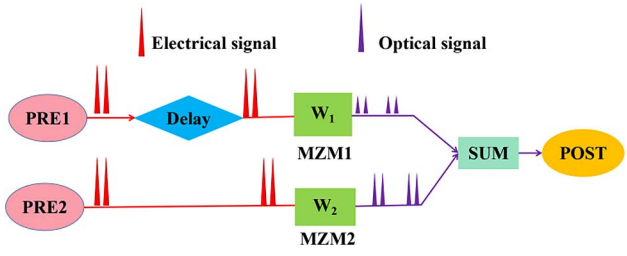

Fig. 1. Schematic diagram of the coherent photonic spiking neural network.

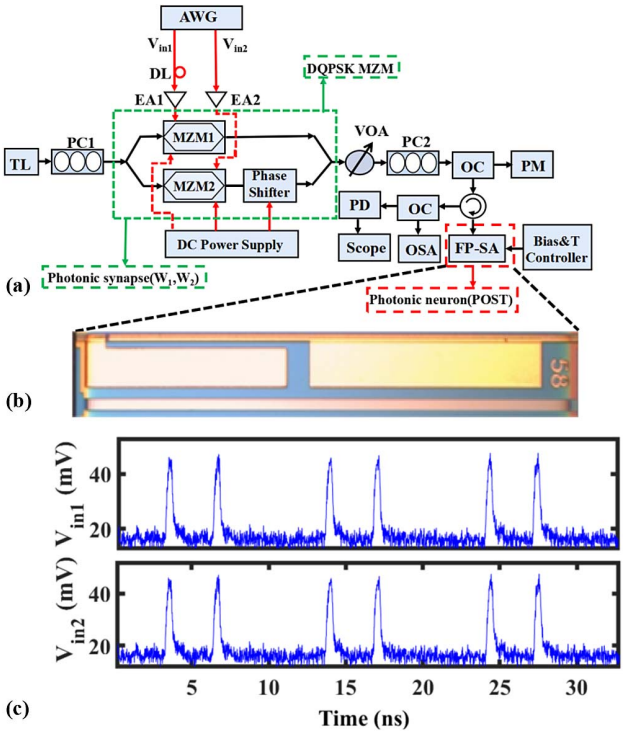

Fig. 2. (a) Experimental setup for the coherent photonic spiking neural network; (b) integrated FP-SA chip and (c) two input signals V_{in1} and V_{in2} generated by AWG. AWG, arbitrary waveform generator; V_{in1} and V_{in2}, input signals; TL, tunable laser; DL, delay line; VOA, variable optical attenuator; PC1 and PC2, polarization controller; EA1 and EA2, electronic amplifier; MZM1 and MZM2, Mach–Zehnder modulator; OC, optical coupler; PD, photodetector; PM, powermeter; OSA, optical spectrum analyzer; Bias&T Controller, bias and temperature controller; Scope, oscilloscope. The black (red) lines correspond to optical (electrical) path. The saturable absorber was reversely biased with the voltage source.

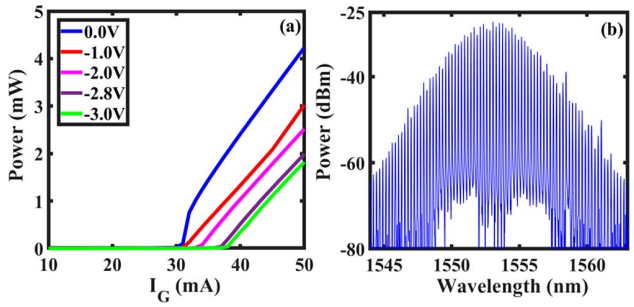

Fig. 3. (a) PI curve and (b) optical spectrum of the FP-SA measured at 25°C. The total length of the FP-SA chip is 1500 μm, the width of the laser chip is 300 μm, the ridge waveguide width is 2.5 μm, and the length of the SA region is 75 μm. The SA section side facet and gain section side facet are coated with reflections of 95% and 30%, respectively.

weighted with two MZMs through the same optical carrier generated by the TL. The weighted sum signal was subsequently injected into the FP-SA. The injected power of the modulated light could be further controlled by the variable optical attenuator (VOA). The output of the FP-SA neuron was split into two paths via an optical coupler, one of which was captured by the optical spectrum analyzer (OSA, Advantest Q8384), and the other was converted to the electrical domain by the means of a photodetector (PD, Agilent/HP11982A) and was subsequently captured by an oscilloscope (OSC, Keysight DSOV334A).

The quantum-well FP-SA behaves analogously to the spiking neuron model. The gain region of the FP-SA is driven by a current source. The saturable absorber (SA) region is driven by a voltage source with reverse voltage. Figure 3(a) depicts the power-current (PI) curves of the FP-SA under various reverse voltage cases of the SA region measured at 25°C. It can be seen that the gain current (I_G) threshold is approximately 30 mA at a reverse voltage of 0 V. Besides, as the SA reverse voltage increases, the threshold current also increases. Figure 3(b) shows the optical spectrum for a free-running FP-SA, showing the multi-longitudinal-mode lasing spectrum. For the FP-SA, with proper gain current and reverse voltage, self-pulsation regimes such as Q switching and mode-locked state can be observed [48,49]. Note that, for the single-mode laser with SA [21,50,51], the excitable behavior occurs just below the lasing threshold; while for the multimode FP-SA [48,52], as indicated in Refs. [48,52], the pulse state is observed above the lasing threshold. Thus, the bias current of the FP-SA laser neuron is above the lasing threshold but below the self-pulsation threshold.

In our proposed coherent photonic spiking neural network, the DQPSK MZM serves as optical synapses and is used for linear weighted summation calculations. Note that, if using two discrete MZMs, unstable interference phenomena can be observed in experiment. To address this stability issue, we employ the integrated DQPSK MZM, which makes the synapse stable. In our experiments, we used a Ti:$LiNbO_3$ DQPSK single-drive MZM (DQPSK MZM) with modulation speed of up to 22.5 Gbaud. As shown in the green box in Fig. 2(a), the DQPSK MZM uses high-speed traveling wave MZMs for linear modulation and a phase shifter for summation operation. In order to accurately bias the two MZMs and the phase shifter, the respective DC power sources are used. V_1 and V_2 are the bias voltages applied to the corresponding MZMs. The constructive interference between two optical signals can be achieved when the phase shift is 0.

3. RESULTS

Here, the proposed coherent photonic neural network is utilized to demonstrate the implementation of both linear and nonlinear computational functions.

At first, we consider the linear weighted summation implemented by the DQPSK MZM. By traversing the bias voltages of the two modulators, we obtain the modulation characteristics of the DQPSK MZM, as shown in Fig. 4. Table 1 represents the one-to-one correspondence between the bias voltages V_1 and V_2 of the two MZMs and the weight values W_1 and W_2 of the neural network. We obtain the desired weighted signals by adjusting the values of V_1 and V_2 to control the weights.

Similar to a biological neuron, the nonlinear computational functions of a photonic spiking neuron mainly include

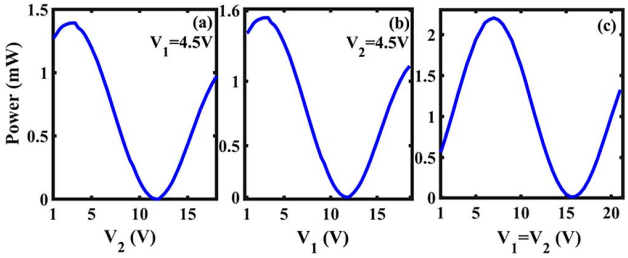

Fig. 4. Modulation characteristics of the DQPSK single-drive MZM. The phase shifter is 0. The bias voltage of MZM1 (MZM2) is V_1 (V_2). (a) $V_1 = 4.5$ V; (b) $V_2 = 4.5$ V; (c) $V_1 = V_2$.

Table 1. Weight Corresponding to the Voltage

V_1 (V)	W_1	V_2 (V)	W_2
3.00	1	3.00	1
5.62	0.8	5.40	0.8
6.91	0.6	6.80	0.6
8.21	0.4	7.90	0.4
9.50	0.2	9.30	0.2
11.36	0	11.00	0

temporal integration, threshold, and refractory period. We have obtained different weighted summation signals by adjusting electrical delay and voltages of the MZMs and phase shifter to demonstrate the implementation of complex nonlinear neuron-like dynamics.

As shown in Fig. 5(a1), the weighted summation signal after electrical delay contains two weak perturbation pulses of the same power and a set of two closely spaced weak pulses. As shown in Fig. 5(a2), by adjusting the delay of the two electrical input signals so that the inter-spike interval (ISI) of two closely spaced weak perturbation pulses is 0.6 ns, the FP-SA neuron is triggered to generate a neuron-like spike, while the remaining perturbation pulses do not produce the response pulses. In other words, although a single weak pulse cannot reach the spike threshold, the two closely spaced weak pulses are temporally integrated and, thus, exceed the threshold, which demonstrates the proposed coherent optical neural network can realize the temporal integration property. To demonstrate that reproducible spiking responses can be obtained in the experiment, we further show the experimental color-coded temporal maps, plotting a superimposed time series of the responses corresponding to 100 successive arriving stimulus events, as shown in Fig. 5(c1). This illustrates that, for each of the 100 incoming stimuli, the same spiking response is obtained. In addition, the effects of the ISI on the temporal integration property are examined carefully. It is found that FP-SA neurons can achieve temporal integration when the interval between external input pulses is between 0.2 and 0.8 ns. As shown in Fig. 5(b1), by adjusting V_1 and V_2, the weighted summation signals consist of three pulses with different powers. Only the second pulse with power above the threshold triggers the FP-SA neuron to generate a spike, whereas the first and third pulses do not generate response spikes because they do not exceed the threshold, as shown in Fig. 5(b2). The experimental measurements indicate that the threshold of V_{in} is about 40 mV. Figure 5(c2) further demonstrates the repeatability of the threshold response.

In order to verify the refractory period property, the optical power of TL is increased so that the value of V_{in} is well above the threshold, as shown in Figs. 6(a1) and 6(b1). As shown in Figs. 6(a1) and 6(a2), the weighted summation signals consist of two strong perturbation pulses and a set of two strong perturbation pulses that are closely spaced. Obviously, a single strong perturbation pulse can elicit a response spike. It is found that the four pulses triggered only three response spikes, which indicates the refractory period. This is because it takes time for

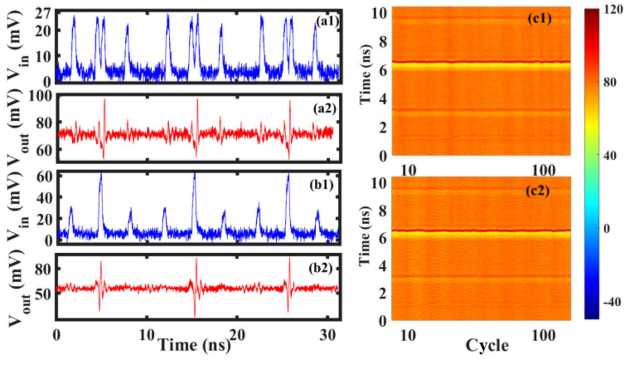

Fig. 5. Experimental demonstration of temporal integration property and spike threshold property. (a1) and (a2) indicate temporal integration property. (a1) represents the input signals for the weighted summation and (a2) denotes the response of the FP-SA neuron. (b1) and (b2) indicate spike threshold property. (b1) represents the input signals for the weighted summation and (b2) denotes the response of the FP-SA neuron. Temporal maps show the laser neuron's responses to 100 successive external stimuli, where (c1) corresponds to the stimulus in (a1) and (c2) to the stimulus in (b1). The bias voltage of the FP-SA is −1.846 V, and the bias current is 62.8 mA.

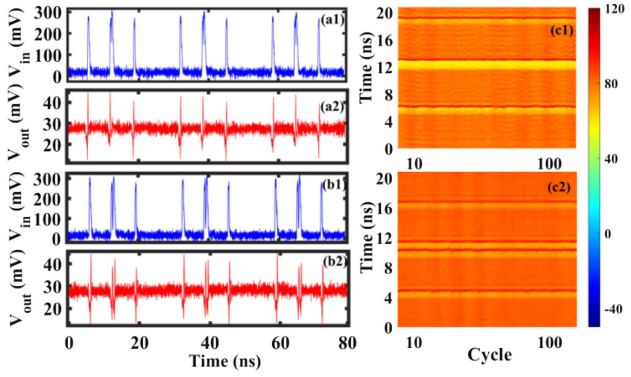

Fig. 6. Experimental demonstration of the refractory period property. (a1) and (a2) indicate that FP-SA neurons are in the refractory period regime. (a1) represents the input signals for the weighted summation and (a2) denotes the response of the FP-SA neuron. (b1) and (b2) indicate that the FP-SA neuron has left the refractory period regime. (b1) represents the input signals for the weighted summation and (b2) denotes the response of the FP-SA neuron. Temporal maps show the laser neuron's responses to 100 successive external stimuli, where (c1) corresponds to the stimulus in (a1) and (c2) to the stimulus in (b1). The bias voltage of the FP-SA is −1.846 V, and the bias current is 62.8 mA.

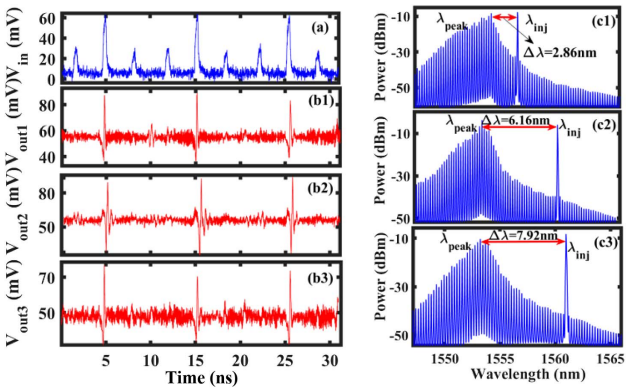

Fig. 7. Experimental demonstration of the effect of frequency detuning on spike threshold property. (a) represents the input stimulus signal. (b1)–(b3) denote the response of the FP-SA neuron, corresponding to the three optical spectra for the FP-SA that operates as a photonic spiking neuron, as shown in (c1)–(c3). The bias voltage of the FP-SA is −1.846 V, and the bias current is 62.8 mA.

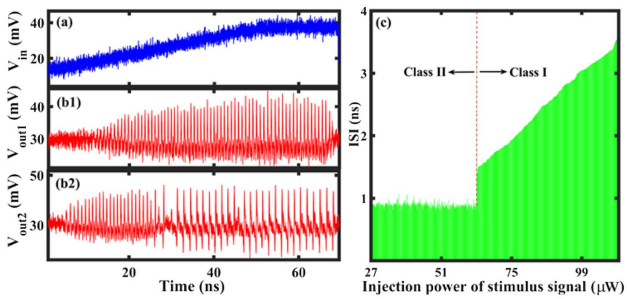

Fig. 8. Spike response of the FP-SA neuron when injecting the triangular stimulus signal. (a) represents the input signal where the light intensity varies as a triangular wave. (b1) and (b2) denote the response of the FP-SA neuron. (c) represents the ISI interval distribution corresponding to the first type of spike and the second type of spike. The bias voltage of the FP-SA is −1.846 V, and the bias current is 62.8 mA.

the gain section to fully recover its gain. Besides, the effects of the ISI on the refractory period property are examined carefully. The FP-SA neuron responds with a single spike when ISI is between 0.2 and 0.5 ns, indicating that the refractory period is about 0.5 ns. When the FP-SA neuron has left the refractory period regime, namely, when the ISI is greater than 0.5 ns, every perturbation pulse can elicit a response spike. As shown in Figs. 6(b1) and 6(b2), when the ISI is 0.6 ns, four pulses triggered four response spikes. The experimental color-coded temporal maps are shown in Figs. 6(c1) and 6(c2), demonstrating that reproducible refractory period property can be obtained in the experiment.

In addition, the effect of the wavelength of the optically injected light on the realization of neuron-like dynamics has been carefully investigated. Figure 7 shows the optical spectra for the optically injected FP-SA that operates as a photonic spiking neuron. The wavelength of the TL is varied so that it is injected into different longitudinal modes of the FP-SA. In particular, the spacing between the wavelength of the external optical stimulus and the peak wavelength of the FP-SA is an integer multiple of the longitudinal mode spacing (0.22 nm for the FP-SA). Here, for the spike threshold property, we select three representative experimental results with distinct wavelength differences (2.86 nm, 6.16 nm, and 7.92 nm) as shown in Fig. 7. Note, it is experimentally demonstrated that neuron-like dynamics can also be achieved when the wavelength of the external optical light is less than the peak wavelength of the FP-SA.

The experimental result verifies that our proposed coherent photonic spiking neural network architecture can achieve linear computation and complex nonlinear neuron-like dynamics. Besides, thanks to the introduction of the delay element, the proposed network architecture is a promising candidate for hardware implementation of the delay-weight learning algorithm [46].

4. DISCUSSION

Note that class I and class II excitabilities are two major categories observed in biological neurons [53]. We further consider the excitability class of the FP-SA neuron. Here, we consider a time-varying stimulus signal and study the spike response. The results are shown in Fig. 8. On the one hand, as shown in Fig. 8(b1), the ISI of the spike train is almost constant, but the spike amplitude is increased with the stimulus strength. According to the bifurcation theory, this may be attributed to the Andronov–Hopf bifurcation, which is related to class II excitability [53,54]. When the FP-SA neuron is in class II excitability, the external optical injection power is around 40 μW, the bias voltage is −1.846 V, and the bias current is 62.8 mA. On the other hand, as shown in Fig. 8(b2), when the injection power is increased, we can see that two different spikes are responding to the triangular stimulus signal. The first type of spike is similar to that shown in Fig. 8(b1), and the second type of spike train has similar spike amplitude, but the ISI is varied with the stimulus strength, which may be attributed to the saddle-node bifurcation or homoclinic bifurcation; thus, it is related to class I excitability [55,56]. When the FP-SA neuron is operating at class I excitability, the bias voltage is −1.846 V, the bias current is 62.8 mA, and the external optical injection power is approximately 60 μW or higher. It is clear that in Fig. 8(b2) the first type of spike response does not have a well-defined threshold, but the second type of spike does. Figure 8(c) represents the ISI distribution with respect to the injection power of stimulus signals. As seen in Figs. 8(b2) and 8(c), although the bias point of the FP-SA does not change, the change in the externally injected optical power causes a switch in the FP-SA state. In other words, as the external optical injection changes, the FP-SA alternates between class I and class II excitability. We, therefore, believe that both excitability mechanisms contribute to the neural-like computational functions. Note that the average optical power value recorded by the optical powermeter serves as the amount of externally injected optical power in our experiments. Thus, we think the FP-SA neuron supports both class I and class II excitability depending on the parameters, which is similar to the findings obtained in Ref. [57]. That is to say, the FP-SA can act as either resonator-type or integrator-type neuron [58].

5. CONCLUSION

We proposed and experimentally demonstrated a prototypical coherent photonic spiking neural network that included the

MZM as the photonic synapse and the FP-SA as the photonic spiking neuron. Both the linear weighted summation and complex nonlinear neuron-like dynamics including temporal integration, threshold, and refractory period were experimentally demonstrated. More specifically, the weighted summation was obtained by means of different delays and modulation indices of the MZM. The nonlinear neuron-like dynamics were achieved in the FP-SA subject to optical injection from the weighted sum of presynaptic signals. In addition, the condition of the spacing between the wavelength of the external optical stimulus and the peak wavelength of the FP-SA for the neuron-like dynamics was revealed. It is suggested that the neuron-like dynamics were attained when the wavelength of the external optical stimulus matches or is slightly larger than the longitudinal mode wavelength of the FP-SA. The proposed approach offers a promising solution to realize the photonic spiking neural network hardware and plays a key foundation for large-scale photonic integrated spiking neural network chips.

Note, to solve complex computation tasks, large-scale photonic spiking neural network (SNN) is further desired. To obtain a fully integrated large photonic spiking neural network, there are still many bottlenecks and difficulties. First, the footprint of the FP-SA neuron and MZM synapse is relatively large, which makes high-density integration difficult. Second, there is no single commercial fabrication platform enabling the light sources, passive and active components being fully integrated in a single chip [59]. Third, the loss, heat dissipation, and thermal cross talk should be carefully addressed. Fourth, the coupling efficiency of the TL, MZM array, and FP-SA array needs to be improved. Fifth, the opto-electronic packaging of large-scale chips is also a considerable challenge [60].

Funding. National Key Research and Development Program of China (2021YFB2801900, 2021YFB2801901, 2021YFB2801902, 2021YFB2801904); National Natural Science Foundation of China (61974177, 61674119); Outstanding Youth Science Fund of National Natural Science Foundation of China (62022062); Fundamental Research Funds for the Central Universities (JB210114).

Disclosures. The authors declare no conflicts of interest.

Data Availability. Data underlying the results presented in this paper are not publicly available at this time but may be obtained from the authors upon reasonable request.

REFERENCES

1. Y. LeCun, Y. Bengio, and G. Hinton, "Deep learning," Nature **521**, 436–444 (2015).
2. W. Zhang, B. Gao, J. Tang, P. Yao, Y. Shimeng, C. Meng-Fan, H.-J. Yoo, H. Qian, and H. Wu, "Neuro-inspired computing chips," Nat. Electron. **3**, 371–382 (2020).
3. F. Akopyan, J. Sawada, A. Cassidy, R. Alvarez-Icaza, and J. Arthur, "TrueNorth: design and tool flow of a 65 mW 1 million neuron programmable neurosynaptic chip," IEEE Trans. Comput. **34**, 1537–1557 (2015).
4. S. B. Furber, D. R. Lester, L. A. Plana, J. D. Garside, E. Painkras, S. Temple, and A. D. Brown, "Overview of the SpiNNaker system architecture," IEEE Trans. Comput. **62**, 2454–2467 (2013).
5. M. Davies, N. Srinivasa, and T.-H. Lin*et al.*et al., "Loihi: a neuromorphic manycore processor with on-chip learning," IEEE Micro **38**, 82–99 (2018).
6. G. W. Burr, "A role for optics in AI hardware," Nature **569**, 199–200 (2019).
7. Y. Shen, N. C. Harris, S. Skirlo, M. Prabhu, T. Baehr-Jones, M. Hochberg, X. Sun, S. Zhao, H. Larochelle, D. Englund, and M. Soljačić, "Deep learning with coherent nanophotonic circuits," Nat. Photonics **11**, 441–447 (2017).
8. G. Wetzstein, A. Ozcan, S. Gigan, S. Fan, D. Englund, M. Soljačić, C. Denz, D. A. B. Miller, and D. Psaltis, "Inference in artificial intelligence with deep optics and photonics," Nature **588**, 39–47 (2020).
9. A. N. Tait, T. F. de Lima, E. Zhou, A. X. Wu, M. A. Nahmias, B. J. Shastri, and P. R. Prucnal, "Neuromorphic photonic networks using silicon photonic weight banks," Sci. Rep. **7**, 7430 (2017).
10. B. Shi, N. Calabretta, and R. Stabile, "Deep neural network through an InP SOA-based photonic integrated cross-connect," IEEE J. Sel. Top. Quantum Electron. **26**, 7701111 (2020).
11. S. Xiang, Z. Ren, Z. Song, Y. Zhang, X. Guo, G. Han, and Y. Hao, "Computing primitive of fully-VCSELs-based all optical spiking neural network for supervised learning and pattern classification," IEEE Trans. Neural Netw. Learn. Syst. **32**, 2494–2505 (2021).
12. Y. J. Lee, M. B. On, X. Xiao, R. Proietti, and S. B. Yoo, "Photonic spiking neural networks with event-driven femtojoule optoelectronic neurons based on Izhikevich-inspired model," Opt. Express **30**, 19360–19389 (2022).
13. E. Yurtsever, J. Lambert, A. Carballo, and K. Takeda, "A survey of autonomous driving: common practices and emerging technologies," IEEE Access **8**, 58443–58469 (2020).
14. A. Graves, A. R. Mohamed, and G. Hinton, "Speech recognition with deep recurrent neural networks," in *IEEE International Conference on Acoustics, Speech and Signal Processing* (2013), pp. 6645–6649.
15. W. T. Miller, "Real-time application of neural networks for sensor-based control of robots with vision," IEEE Trans. Syst. **19**, 825–831 (1989).
16. V. Sze, Y. H. Chen, J. Emer, A. Suleiman, and Z. Zhang, "Hardware for machine learning: challenges and opportunities," in *IEEE Custom Integrated Circuits Conference (CICC)* (IEEE, 2017), pp. 1–8.
17. A. Amir, B. Taba, D. Berg, T. Melano, J. McKinstry, C. Di Nolfo, and D. Modha, "A low power, fully event-based gesture recognition system," in *Proceedings of the IEEE Conference on Computer Vision and Pattern Recognition* (2017), pp. 7243–7252.
18. C. D. Schuman, S. R. Kulkarni, M. Parsa, J. P. Mitchell, and B. Kay, "Opportunities for neuromorphic computing algorithms and applications," Nat. Comput. Sci. **2**, 10–19 (2022).
19. P. R. Prucnal, B. J. Shastri, T. F. D. Lima, M. A. Nahmias, and A. N. Tait, "Recent progress in semiconductor excitable lasers for photonic spike processing," Adv. Opt. Photon. **8**, 228–299 (2016).
20. B. J. Shastri, M. A. Nahmias, A. N. Tait, A. W. Rodriguez, B. Wu, and P. R. Prucnal, "Spike processing with a graphene excitable laser," Sci. Rep. **6**, 19126 (2016).
21. M. A. Nahmias, B. J. Shastrin, A. N. Tait, and P. R. Prucnal, "A leaky integrate-and-fire laser neuron for ultrafast cognitive computing," IEEE J. Sel. Top. Quantum Electron. **19**, 1800212 (2013).
22. W. Coomans, L. Gelens, S. Beri, J. Danckaert, and G. Van der Sande, "Solitary and coupled semiconductor ring lasers as optical spiking neurons," Phys. Rev. E **84**, 036209 (2011).
23. A. Hurtadoa, K. Schires, I. D. Henning, and M. J. Adams, "Investigation of vertical cavity surface emitting laser dynamics for neuromorphic photonic systems," Appl. Phys. Lett. **100**, 103703 (2012).
24. Y. Zhang, S. Xiang, X. Guo, A. Wen, and Y. Hao, "Polarization-resolved and polarization-multiplexed spike encoding properties in photonic neuron based on VCSEL-SA," Sci. Rep. **8**, 16095 (2018).
25. R. Wang, C. Qian, Q. Ren, and J. Zhao, "Optoelectronic neuromorphic system using the neural engineering framework," Appl. Opt. **56**, 1517–1525 (2017).
26. S. Barbay, R. Kuszelewicz, and A. M. Yacomotti, "Excitability in a semiconductor laser with saturable absorber," Opt. Lett. **36**, 4476–4478 (2011).

27. C. Mesaritakis, A. Kapsalis, A. Bogris, and D. Syvridis, "Artificial neuron based on integrated semiconductor quantum dot mode-locked lasers," Sci. Rep. **6**, 39317 (2016).
28. S. Xiang, Y. Zhang, J. Gong, X. Guo, L. Lin, and Y. Hao, "STDP-based unsupervised spike pattern learning in a photonic spiking neural network with VCSELs and VCSOAs," IEEE J. Sel. Top. Quantum Electron. **25**, 1700109 (2019).
29. T. Deng, J. Robertson, and A. Hurtado, "Controlled propagation of spiking dynamics in vertical-cavity surface-emitting lasers: towards neuromorphic photonic networks," IEEE. J. Sel. Top. Quantum Electron. **23**, 1800408 (2017).
30. J. Robertson, T. Deng, and J. Javaloyes, "Controlled inhibition of spiking dynamics in VCSELs for neuromorphic photonics: theory and experiments," Opt. Lett. **42**, 1560–1563 (2017).
31. B. Romeira, R. Avó, J. M. Figueiredo, S. Barland, and J. Javaloyes, "Regenerative memory in time-delayed neuromorphic photonic resonators," Sci. Rep. **6**, 19510 (2016).
32. B. Romeira, J. M. L. Figueiredo, and J. Javaloyes, "Delay dynamics of neuromorphic optoelectronic nanoscale resonators: perspectives and applications," Chaos **27**, 114323 (2017).
33. V. A. Pammi, K. Alfaro-Bittner, M. G. Clerc, and S. Barbay, "Photonic computing with single and coupled spiking micropillar lasers," IEEE J. Sel. Top. Quantum Electron. **26**, 1500307 (2020).
34. F. Selmi, R. Braive, G. Beaudoin, I. Sagnes, R. Kuszelewicz, and S. Barbay, "Temporal summation in a neuromimetic micropillar laser," Opt. Lett. **40**, 5690–5693 (2015).
35. J. K. George, A. Mehrabian, R. Amin, J. Meng, T. F. de Lima, A. N. Tait, B. J. Shastri, T. El-Ghazawi, P. R. Prucnal, and V. J. Sorger, "Neuromorphic photonics with electro-absorption modulators," Opt. Express **27**, 5181–5191 (2019).
36. A. N. Tait, T. F. de Lima, M. A. Nahmias, H. B. Miller, H.-T. Peng, B. J. Shastri, and P. R. Prucnal, "Silicon photonic modulator neuron," Phys. Rev. A **11**, 064043 (2019).
37. A. N. Tait, M. A. Nahmias, B. J. Shastri, and P. R. Prucnal, "Broadcast and weight: an integrated network for scalable photonic spike processing," J. Lightwave Technol. **32**, 3427–3439 (2014).
38. J. Feldmann, N. Youngblood, M. Karpov, H. Gehring, X. Li, M. Stappers, M. Le Gallo, X. Fu, A. Lukashchuk, A. S. Raja, J. Liu, C. D. Wright, A. Sebastian, T. J. Kippenberg, W. H. P. Pernice, and H. Bhaskaran, "Parallel convolutional processing using an integrated photonic tensor core," Nature **589**, 52–58 (2021).
39. C. Huang, S. Bilodeau, T. F. de Lima, A. N. Tait, P. Y. Ma, E. C. Blow, A. Jha, H.-T. Peng, B. J. Shastri, and P. R. Prucnal, "Demonstration of scalable microring weight bank control for large-scale photonic integrated circuits," APL Photon. **5**, 040803 (2020).
40. H. Zhang, M. Gu, X. D. Jiang, J. Thompson, H. Cai, S. Paesani, R. Santagati, A. Laing, Y. Zhang, M. H. Yung, Y. Z. Shi, F. K. Muhammad, G. Q. Lo, X. S. Luo, B. Dong, D. L. Kwong, L. C. Kwek, and A. Q. Liu, "An optical neural chip for implementing complex-valued neural network," Nat. Commun. **12**, 457 (2021).
41. G. Mourgias-Alexandris, A. Totovic, A. Tsakyridis, N. Passalis, K. Vyrsokinos, A. Tefas, and N. Pleros, "Neuromorphic photonics with coherent linear neurons using dual-IQ modulation cells," J. Lightwave Technol. **38**, 811–819 (2020).
42. G. Mourgias-Alexandris, M. Moralis-Pegios, S. Simos, G. Dabos, N. Passalis, M. Kirtas, T. Rutirawut, F. Y. Gardes, A. Tefas, and N. Pleros, "A silicon photonic coherent neuron with 10GMAC/sec processing line-rate," in *Optical Fiber Communication Conference* (2021), paper Tu5H.1.
43. B. J. Shastri, A. N. Tait, T. F. de Lima, W. H. P. Pernice, H. Bhaskaran, C. D. Wright, and P. R. Prucnal, "Photonics for artificial intelligence and neuromorphic computing," Nat. Photonics **15**, 102–114 (2021).
44. M. Reck, A. Zeilinger, H. J. Bernstein, and P. Bertani, "Experimental realization of any discrete unitary operator," Phys. Rev. Lett. **73**, 58–61 (1994).
45. H. Zhou, Y. Zhao, X. Wang, D. Gao, J. Dong, and X. Zhang, "Self-configuring and reconfigurable silicon photonic signal processor," ACS Photon. **7**, 792–799 (2020).
46. Y. N. Han, S. Y. Xiang, Z. X. Ren, C. T. Fu, A. J. Wen, and Y. Hao, "Delay-weight plasticity-based supervised learning in optical spiking neural networks," Photon. Res. **9**, B119–B127 (2021).
47. J. Xiang, Y. Zhang, Y. Zhao, X. Guo, and Y. Su, "All-optical silicon microring spiking neuron," Photon. Res. **10**, 939–946 (2022).
48. L. Hou, M. Haji, J. Akbar, B. Qiu, and A. C. Bryce, "Low divergence angle and low jitter 40 GHz AlGaInAs/InP 1.55 μm mode-locked lasers," Opt. Lett. **36**, 966–968 (2011).
49. S. Xiang, Y. Shi, X. Guo, Y. Zhang, H. Wang, D. Zheng, Z. Song, Y. Han, S. Gao, S. Zhao, B. Gu, H. Wang, X. Zhu, L. Hou, X. Chen, W. Zheng, X. Ma, and Y. Hao, "Hardware-algorithm collaborative computing with photonic spiking neuron chip based on integrated Fabry–Pérot laser with saturable absorber," arXiv, arXiv:2204.08362 (2022).
50. F. Selmi, R. Braive, G. Beaudoin, I. Sagnes, R. Kuszelewicz, and S. Barbay, "Relative refractory period in an excitable semiconductor laser," Phys. Rev. Lett. **112**, 183902 (2014).
51. J. L. Dubbeldam, B. Krauskopf, and D. Lenstra, "Excitability and coherence resonance in lasers with saturable absorber," Phys. Rev. E **60**, 6580–6588 (1999).
52. J. Javaloyes and S. Balle, "Mode-locking in semiconductor Fabry-Pérot lasers," IEEE J. Quantum Electron. **46**, 1023–1030 (2010).
53. E. M. Izhikevich, *Dynamical Systems in Neuroscience* (MIT, 2007).
54. G. Kozyreff and T. Erneux, "Singular Hopf bifurcation to strongly pulsating oscillations in lasers containing a saturable absorber," Eur. J. Appl. Math. **14**, 407–420 (2003).
55. B. Krauskopf, K. Schneider, J. Sieber, S. Wieczorek, and M. Wolfrum, "Excitability and self-pulsations near homoclinic bifurcations in semiconductor laser systems," Opt. Commun. **215**, 367–379 (2003).
56. J. L. A. Dubbeldam and B. Krauskopf, "Self-pulsations of lasers with saturable absorber: dynamics and bifurcations," Opt. Commun. **159**, 325–338 (1999).
57. G. Sarantoglou, M. Skontranis, A. Bogris, and C. Mesaritakis, "Experimental study of neuromorphic node based on a multiwaveband emitting two-section quantum dot laser," Photon. Res. **9**, B87–B95 (2021).
58. E. M. Izhikevich, "Resonate-and-fire neurons," Neural Networks **14**, 7883–7894 (2001).
59. X. Guo, J. Xiang, Y. Zhang, and Y. Su, "Integrated neuromorphic photonics: synapses, neurons, and neural networks," Adv. Photon. Res. **2**, 2170019 (2021).
60. Y. Hao, S. Xiang, G. Han, J. Zhang, X. Ma, Z. Zhu, X. Guo, Y. Zhang, Y. Han, Z. Song, Y. Liu, L. Yang, H. Zhou, J. Shi, W. Zhang, M. Xu, W. Zhao, B. Pan, Y. Huang, Q. Liu, Y. Cai, J. Zhu, X. Ou, T. You, H. Wu, B. Gao, Z. Zhang, G. Guo, Y. Chen, Y. Liu, X. Chen, C. Xue, X. Wang, L. Zhao, X. Zou, L. Yan, and M. Li, "Recent progress of integrated circuits and optoelectronic chips," Sci. China Inf. Sci. **64**, 201401 (2021).